TriRod: a 3-<u>R</u>F continuum parallel robot for shape-based load estimation

Matyas Diezinger[1], Brahim Tamadazte[2], and Guillaume J. Laurent[1]

Abstract— In this letter, we will discuss the design, modelling, and estimation of load based on the shape of a newly developed parallel continuum robot called TriRod. The proposed kinematic architecture consists of three flexible rods attached at their lower extremity to three rotating actuators. The robot is able to move its end-effector in space and its three limbs are designed so that their shapes can easily be visible by cameras. Two shape-based estimation strategies have been developed and evaluated experimentally using the TriRod robot. Both estimators are based on virtual visual servoing of the robot rod shapes (deformation) to estimate either the joint angular values or the external forces. The experimental validations show that both estimators give accurate predictions of angles and forces, with a mean average error of 3.8% for joint value estimation over a range of $75°$ and a mean average error of 10.5% for the estimation of loads up to $633mN$.

Index Terms— Continuum robot, parallel mechanisms, load estimation, and shape servoing.

I. INTRODUCTION

Parallel Continuum Robots (PCR) are emerging as a novel robotic concept with the potential to be used across a wide range of applications from medical to industrial [?]. Like parallel robots, PCRs consist of several independent limbs actuated at their base and attached at their end to a rigid platform which can be considered as the end-effector. However, unlike parallel robots, PCRs' kinematics chains integrate slender flexible elements in place of or in combination with rigid links.

Several PCRs architectures have been proposed in the past few years providing from two to six degrees of freedom (DoF) to the end effector. Planar structures consist of two or three limbs positioned in the same plane able to move the end-effector (X, Y, and Θ) [?], [?], [?], [?], [?]. To move the end-effector in the space, many structures have been proposed from three parallel limbs [?], [?], [?], [?] to six limbs [?], [?], [?], [?]. In both cases, the limbs of the PCRs are either passive (with extrinsic actuation) as proposed in [?] or active (with intrinsic actuation) [?]. Most of PCR moving in 3D are actuated from translating their limbs [?], [?], [?] as an efficient way to obtain out-of-plane movements of the end-effector.
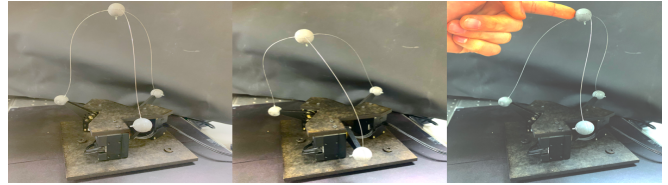
Fig. 1. Shape and load deformation of the continuum parallel robot "TriRod".

PCRs have several advantages compared to traditional parallel robots. The first one is the increase in the workspace thanks to the flexibility of the limbs providing large deformations [?], [?]. Another benefit is the capability to miniaturize deformable parallel structures compared to rigid ones. This has been demonstrated for example in [?] that removing mechanical joints and transmission, it was possible to miniaturize a six DoFs parallel mechanism within a few cube centimeters [?]. Mauze et *al.* [?] investigated the use of purely elastic materials in the design of a PCR which has shown very good performance in terms of precision. Additionally, it has been evidenced that the compliant nature of PCRs confers safer interactions with humans for collaborative tasks [?], [?], [?].

Conversely, the flexibility of PCRs reduces the forces and moments that can be applied at their end-effector. The payload of these robots is then much lower than their rigid counterpart. The most critical problem is guaranteeing the robot's trajectory under different payloads or external forces in general. Obviously, physical models of PCRs allow estimating the actuator's position or orientation to reach a desired pose in the Cartesian space. However, whether the external loads are unknown, the models cannot predict the end-effector position. Indeed, the pose of PCRs is highly dependent on unpredictable external interactions.

A solution is to use the flexible nature of PCRs to enable sensing of interaction forces using the deflection of the robot itself as proposed by Aloi et *al.* [?]. As all the PCRs have in common the use of flexible limbs in place of rigid links, then their deformations are the direct reflection of external forces. Consequently, the resulting deformation of the limbs, therefore, the robot shape can be used to estimate interactions. These deformations can be estimated either with proprioceptive sensors or with exteroceptive sensors. Among the firsts, strain gauges [?], pressure sensors [?], Bragg's fibres [?], [?], cable tension sensors [?], [?] and other types of sensors have already been used through these on-board sensors require much

space and modifications on PCRs. On the other hand, exteroceptive sensors like magnetic sensors [?], [?] or visual sensors [?], [?] allow shape measurements without modification of the PCRs. The use of vision-based deformation measurement to estimate external forces has been validated efficiently on catheter-like continuum robot [?], [?], [?] or soft pneumatic parallel robots [?] but to our knowledge not on parallel continuum robot with beam legs.

This paper discusses a PCR mechanism specifically designed to study the sensing of interaction forces using vision, named TriRod. The TriRod robot consists of three flexible rods attached at their lower extremity to three rotating actuators. The robot is able to move its end-effector in space and its three limbs are designed so that their shapes can be entirely retrieved by visual sensors. A model-based force estimation method suitable for continuum parallel structures is proposed and validated with applications to the TriRod.

The paper begins with the presentation of the design, the modelling, and the analysis of the TriRod. These analyses have been performed to assess the workspace and stiffness when the robot is subjected or not to external loads. Then, two vision-based estimation strategies are introduced. The first retrieves the configuration (i.e., shape) of the robot, while the second estimates the external forces applied to its end-effector. Both estimators are based on virtual visual servoing of the robot rod shapes (i.e., deformation). Finally, the paper ends with experimental validations showing that both estimators give accurate predictions of positions and forces.

II. DESIGN AND MODELLING OF THE TRIROD ROBOT

A. Mechanical Design and Fabrication

This section describes the design and modelling of the proposed three DoFs TriRod robot which is a parallel continuum robot with three deformable legs (rods). Each individual rod is attached at its lower extremity to a rotating actuator which, given the robot's design, can vary from 0 to $\frac{\pi}{2}$. The three rods are fixed on a sphere which is the end effector of the TriRod. Finally, the three rotating actuators are positioned with an angle of $\frac{2\pi}{3}$ in respect to each other. Figure 2 depicts the kinematic diagram of the proposed robot as well as the used frames and geometrical parameters. The geometrical parameters have been chosen to allow large deformations of the legs. Note that depending on the intended robotic task, the rods can be changed (material, length, diameter, etc.) for a trade-off of wide working space/low stiffness or small working space/high stiffness. The TriRod provides 3 DoFs to the end-effector with a resolution of 0.1 mm and a maximum speed of 5.2 $mm.s^{-1}$. It can support a weight of up to 75 g for the example of robot shown in Fig. 1.

Each rod is actuated with a Dynamixel XM430-W210-R servomotor providing an angular resolution of 4096 $pulse.rev^{-1}$. To allow a higher range of motion for the robot end-effector, each rod is mounted on a rigid

aluminium-made arm which is itself mounted on the motor. The rods are made of flexible steel spring rods of 1 mm in diameter and 185 mm in length. The three servomotors are fixed with an angle of $\frac{2\pi}{3}$ from each other and at a distance $r = 40$ mm of the centre O. The length of the rigid arm is $d = 50$ mm. At a standstill, i.e. when the rigid arms are horizontal with an angle of 0°, the TriRod's height from the XY plan formed by the points A_1, A_2, A_3 to the end effector C is of 160 mm (Fig. 2). The distance between two points B_i and B_j, $i, j \in [1, 2, 3], i \neq j$ is 180 mm in the same configuration.
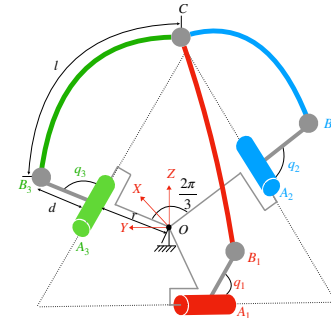

Fig. 2. Kinematic scheme of the TriRod robot and its geometric parameters.

Once the different components are assembled, the obtained robot is characterized geometrically using metrology equipment. Therefore, the geometric parameters d and l are measured with an accuracy of 0.05 mm using a high gauge and a calliper, whereas the other distances such as r are measured with a coordinate measuring machine with an accuracy of 0.02 mm. The mechanical and dimensional inaccuracies are then included in the robot model discussed hereinafter.

B. Kinematic Modelling

Parallel robots with rigid transmission mechanisms have been widely investigated in the literature from the design, modelling and control aspects [?]. However, the modelling of PCRs requires numerical methods to solve partial differential equations of continuum mechanics. Different methods can be approached to model PCRs. Piece-wise continuous curvature modelling offers simplicity and fast estimations for regular structures, however, it may be lacking in precision for nonlinear deformation. On the other hand, shooting methods based on beam equations provides high accuracy by considering nonlinearities and material properties, but requires more computational effort and may show convergence issues. Lastly, finite element modelling is a more flexible approach offering precise modelling of complex and nonlinear deformations, and accounting for material properties. However, it demands high computational resources as the accuracy depends on the mesh size. While other methods can also be considered, the TriRod is modelled using Finite Element Analysis (FEA) due to its high accuracy and capability to model complex multi-beam structures. In

this paper, we have opted for an FEA software named SOFA (Simulation Open Framework Architecture) [?]. SOFA allows the modelling and simulation of physical systems of different types, materials, and shapes.

The TriRod system is modelled using finite beam elements [?]. Each of the three legs is represented as a flexible rod divided into ten sections with hundred interpolation points, enabling forward computation of the robot pose.

C. Workspace Analysis

The workspace of the TriRod is defined as the space area that the end effector can cover when the servomotors' angles $\mathbf{q}_i = (q_1, q_2, q_3)^\top$ vary from vertical to horizontal positions (respectively 0 and $\frac{\pi}{2}$), without considering the plastic deformations of the rods. The workspace boundaries are imposed either by a physical limitation of the actuator angles or at the position where the flexible rods reach the yield point. As a reminder, the used rods are made with steel spring rods, which have a flexural yield point of 3.6×10^9 Pa. Let us consider two different configurations to define the workspace. On one hand, a load-free operation where the position of the end effector C is subject only to the motion of the actuator and on the other hand, a constrained operating where an external force is applied to the robot mobile platform C.

1) Unconstrained Workspace Analysis: To evaluate the positions of the robot end-effector, we generated a grid of 8^3 possible combinations of actuator angular positions by dividing the stroke of every actuator into 8 steps from 0 to $\frac{\pi}{2}$. Thereby, for each triplet of discretized angular position, the obtained position c_p of the robot end-effector is recorded and plotted. The maximum stress in the whole model is also computed in each discrete position from the curvatures of the flexible rods to ensure that the yield point is never reached. This stress is represented by the colour scale in Fig. 3.
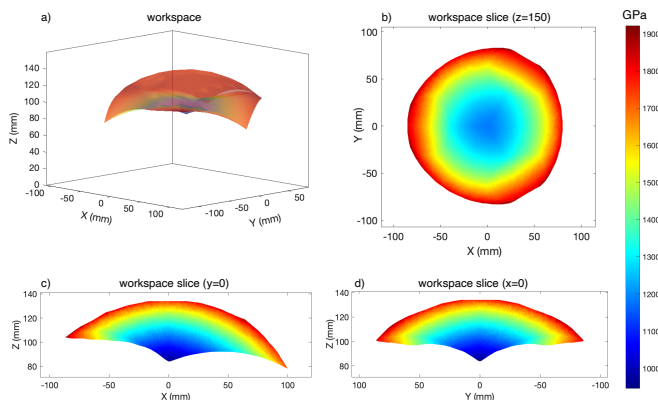

Fig. 3. Workspace analysis of the TriRod robot. (a) the reachable workspace in a perspective view, (b) a top view of the workspace at $Z = 150$ mm, c) the workspace along the X-axis, while d) the one obtained along the Y-axis.

As can be expected from the geometry of the TriRod, the workspace presents a symmetry with respect to the XZ-plane (Fig. 3(d)). In the case where there is no external

force acting on the robot, there is a clear symmetry of $\frac{2\pi}{3}$ around Z-axis in the TriRod geometry as well as in its workspace (Fig. 3(b)) and in the distribution of the maximum stress. Despite experiencing stress peaks in configurations far from the centre of the workspace, the yield point is never reached, thus avoiding the risk of degradation. However, it is required to prevent the TriRod from reaching high internal stresses. In an isotropic continuum structure, instabilities generally occur in response to significant variations in applied stresses. For instance, when the TriRod reaches the upper limits of its workspace where stresses are highest, instability can appear as spontaneous torsion of the entire robot. To avoid these instabilities like torsion and buckling, high-stress areas are made inaccessible by limiting the actuator's range of motion.

2) Constrained Workspace: One of the advantages of a continuous parallel robot is to use compliance to change its working space function of the applied external force. Indeed, it is possible to change the shape of the rods by applying an external force $\mathbf{f}_{ext}$ on the platform. To evaluate such a statement, an external force has been applied at the robot's end-effector at each position of the workspace. New spatial positions can be reached under external loads, leading to new workspaces. A range of external forces is used to assess the potential impact of the applied forces on the extent of the working space. Examples of constrained workspace slices are superposed in Fig. 4 corresponding to external loads of 0.5 N along the directions X, Y, and Z, respectively. As can be seen in this figure, the complete workspace is translated in the direction of the external force, allowing the TriRod to reach a farther portion of the space around itself but preventing it to reach a portion of space on the opposite side. The constrained workspaces are also longer and narrower than the force-free workspace. This flexibility gives the robot an interesting versatility, as when the end effector meets an obstacle, it takes a new direction out of the original working space. However, the TriRod robot is not designed to fully exploit the versatility of its workspace. It is only necessary to consider the potential modifications of this workspace to fully characterize the robot and ensure a comprehensive understanding of the extended limits of its workspace.

D. Stiffness Evaluation

The TriRod behaviour under external loads is highly dependent on its configuration and the materials used to build the robot. The occurring deformations and the involved forces are directly related to the stiffness. The TriRod stiffness can be characterized by the motion resulting from loads carried by the robot's end-effector in different directions (X, Y, Z). Thereby, the directional stiffness K_x, K_y, and K_z are expressed as functions of the angular positions of the actuators. To this end, we simulated the displacements δ of the robot platform subjected to an external force $\mathbf{f}_{ext}$ of 0.1 N for each
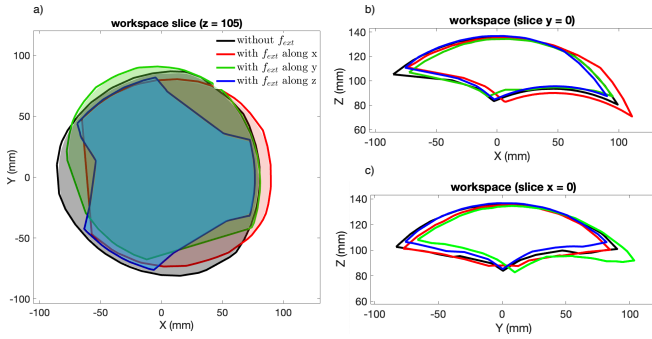
Fig. 4. Comparison of load-free workspace and three constrained workspaces, i.e. by applying external forces along X, Y and Z: a) shows the obtained workspaces in the slice $Z = 105$, b) in the slice $Y = 0$ and c) in the slice $X = 0$.

direction. The corresponding stiffness K is estimated as follows (1):

$$K = \frac{\|\mathbf{f}_{ext}\|}{\delta} \tag{1}$$

Figure 5 depicts the analysis of the TriRod stiffness. Note that the first leg of the TriRod is moving in the XZ-plane as its actuator is rotating around the Y-axis. Therefore, as expected the stiffness K_x along the X-axis (Fig. 5(a)) is much higher near this actuator because the corresponding flexible leg has a narrow S-shape acting like a spring. On the other side, the stiffness K_y along the Y-axis (Fig. 5(d)) is higher when the end effector is at a lower and centred position because the second and third legs are forming buttresses maintaining the structures. Finally, the main effect of position on stiffness is shown in Fig. 5(d) and (e). The stiffness K_z along the Z-axis is much higher at the top of the workspace than anywhere else as a vertical external load is mainly resulting in compression forces in the direction of the leg centre lines. This compression of the robot decreases significantly as the robot moves away from the perfectly vertical position. Also, as can be noticed from Fig. 5(c), the stiffness along the Z-axis shows a symmetry of $\frac{2\pi}{3}$, with a slightly lower value in between the actuators.
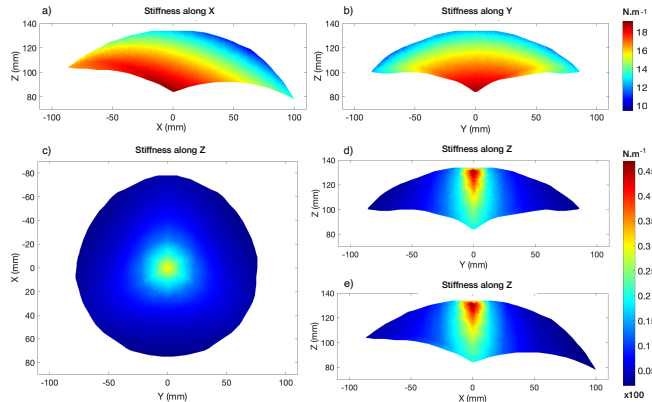

Fig. 5. Stiffness analysis of the TriRod. a) Stiffness K_x in XZ plane. b) Stiffness K_y in YZ plane. c) Stiffness K_z in XY plane. d) Stiffness K_z in YZ plane. e) Stiffness K_z in XZ plane.

III. SHAPE-BASED LOAD ESTIMATION

A. Objectives

This section focuses on the design of the proposed vision-based estimation schemes of both the position and the applied external forces. Indeed, these estimation frameworks allow 1) estimating the input joint angular values (Fig. 6) using the robot posture (shape) and 2) estimating an external load applied at the end effector in a fixed configuration (Fig. 7). Both challenges introduced above are tackled with closed-loop vision-based estimation schemes that are well suited for such tasks, notably for their robustness to various types of errors. The principle of the estimation schemes consists of deforming the body of the robot model from an initial posture towards the posture of the real TriRod either by changing the joint angles or adding an external load (respectively, applying an external force). A visual similarity criteria based on mutual information was investigated to estimate the difference in the posture of the legs.

B. Estimation Schemes

As already pointed out, it is not trivial to adequately express the kinematic models of such an architecture. However, SOFA provides a very accurate numerical model fully suitable for control purposes. Therefore, an original estimation scheme has been developed based on the simultaneous use of a pair of virtual cameras that visualize the numerical SOFA model and another pair of real cameras that view the physical robot. The extrinsic parameters of the real cameras are used to position the virtual cameras in the SOFA framework to ensure the same views of the robot. Afterwards, the deformed shape of the TriRod is projected into the image $\mathbf{I}_{r,1}$ and $\mathbf{I}_{r,2}$ using the real cameras and without any 3D reconstruction procedure. In parallel, the same procedure is also applied to the equivalent numerical robot whose shape is projected into the images $\mathbf{I}_{m,1}$ and $\mathbf{I}_{m,2}$. The difference between the real and virtual images is used to compute the estimated input values of the model.

Two alternatives of the shape-based estimator are proposed. The first method consists of estimating the joint angles (q_1, q_2, q_3) without any external forces which means that the robot does not carry a load (i.e., force-free functioning mode) (Fig. 6). The TriRod's pose $\mathbf{p}_r$ is recovered using the cameras and compared to the model's pose $\mathbf{p}_m$ with a shape comparator described in Section III-C. The resulting similarity criterion ϵ is used in a minimization algorithm described in Section III-D to compute the guess joint inputs $\hat{q}_1, \hat{q}_2, \hat{q}_3$.

The second method investigates the estimation of an unknown load applied to the TriRod end-effector. This means moving manually the robot end-effector by applying an external force $\mathbf{f}_{ext}$ when the actuators without moving using the actuators. Thus, the objective is now to compute an estimation $\hat{\mathbf{f}}_{ext}$ of the applied load that produces the estimated deformed shape of the robot using
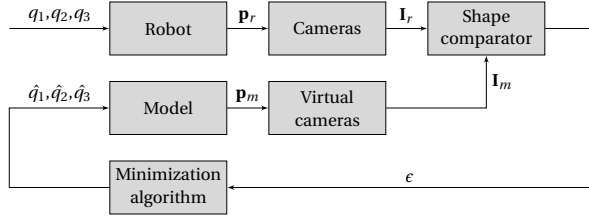
Fig. 6. Shape-based joint estimation scheme: $\mathbf{q}_i$ is the input of the angular actuator i, $\mathbf{p}_r$ the 3D pose of the TriRod robot, $\mathbf{I}_r$ the 2D images of the TriRod, $\mathbf{p}_m$ the 3D pose of the numerical model, and $\mathbf{I}_m$, the 2D images of the model.

by comparing both involved shape due to the applied load and the initial shape as depicted in (Fig. 7).
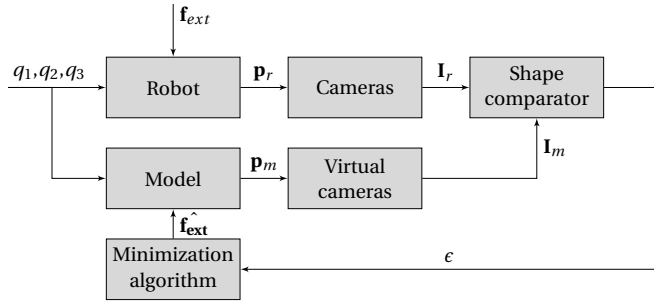

Fig. 7. Shape-based force estimation scheme.

C. Visual Features and Similarity criterion

1) Images Preprocessing: As the TriRod's shape is tridimensional, it is required to use two cameras to be able to view the whole robot including the hidden parts. Note that it is not necessary to reconstruct in 3D the robot, which can be a relevant solution but is complex (need accurate calibration) and time-consuming, therefore not compatible with the real-time aspects. Indeed, the shape of the TriRod is projected in the two images $I_{r,1}$, $I_{r,2}$ issued from the real cameras while the shape of the digital model is projected in the two images $I_{m,1}$, $I_{m,2}$ issued from the virtual cameras. Therefore the comparison of shapes can be performed frame by frame with each new acquisition, with a similarity value for each pair of physical/numerical images. The final similarity criterion is chosen to be the sum of the similarity value for each pair. The real images and the virtual ones are processed with some simple basic image processing methods in order to be comparable. Note that the images of the SOFA model are in the form of binary matrices, while the real images are of grayscale type. Therefore, the virtual images are expressed as distance maps using (2) in such a way each background pixel receives the value of the minimal distance to the closest pixel belonging to a rod.

$$\mathbf{I}_{DM}(i,j) = \min_{k,l \ | \ \mathbf{I}(k,l)=255}\left((i-k)^2 + (j-l)^2\right) \quad (2)$$

where $\mathbf{I}_{DM}$ is the distance map image and (i,j) are any pixel coordinates of $\mathbf{I}$.

The real images are acquired under lighting conditions so that the corresponding pixels of the rods are clear on a black background. Indeed, we have selected contrasting materials (i.e., lighter rods on a darker background) to facilitate the image processing stage.

2) Mutual information (MI): The chosen similarity criterion is mutual information which is widely used in information theory [**?**]. It consists of a measure of image similarity although the images are not fully resembling. The estimation of MI between two images is mainly based on two concepts: Shannon entropy and joint histograms.

Let us consider $E(\mathbf{I})$ as the entropy which measures the variability of pixels intensities in an image $\mathbf{I}$ which can be computed as as given in (3).

$$E(\mathbf{I}) = -\sum_{i=0}^{Nc} p_{\mathbf{I}}(i)\log\left(p_{\mathbf{I}}(i)\right) \quad (3)$$

where i is a pixel intensity of $\mathbf{I}(x)$ $\left(i \in [0,255]\right)$ and $p_{\mathbf{I}}(i) = P_r\left(\mathbf{I}(x) = i\right)$ is the probability distribution function of i. Note that in our case, the entropy can be considered as a dispersion measure of the image histogram.

The shared information between two images $\mathbf{I}_r$ and $\mathbf{I}_m$ can be measured using the joint entropy function expressed in (4) which defines the variability between the pair images $(\mathbf{I}_r, \mathbf{I}_m)$.

$$E(\mathbf{I}_r, \mathbf{I}_m) = -\sum_{i=0}^{Nc}\sum_{j=0}^{Nc} p_{\Pi}(i,j)\log\left(p_{\Pi}(i,j)\right) \quad (4)$$

where $p_{\Pi}(i,j) = P_r(\mathbf{I}_r = i \bigcap \mathbf{I}_m = j)$ is the joint probability distribution function. This means that if the joint histogram is low then the images share a large amount of information, i.e., the images are aligned and *vice-versa*.

Finally, the mutual information ϵ_{MI} for a pair of images $(\mathbf{I}_r, \mathbf{I}_m)$ which measures the quantity of shared information can be computed as given in (5).

$$\epsilon_{MI} = -E(\mathbf{I_r}) - E(\mathbf{I_m}) + E(\mathbf{I}_r, \mathbf{I}_m) \quad (5)$$

which can be simplified into:

$$\epsilon_{MI} = \sum_{i=0}^{Nc}\sum_{j=0}^{Nc} p_{\Pi}(i,j)\log\left(\frac{p_{\Pi}(i,j)}{p_{\mathbf{I}_r}(i)\,p_{\mathbf{I}_m}(j)}\right) \quad (6)$$

D. Minimization Procedure

The vision-based estimator is operated alongside a finite element model built on SOFA. This model is running at high speed (60 Hz), allowing the evaluation of several points at each iteration to have an estimation of the local behaviour of the robot at every position without having to operate the hardware robot. Therefore it is possible to evaluate the Jacobian and minimize the similarity criterion with a gradient descent algorithm to match the shapes. However, it is more advantageous to use the Nelder and Mead simplex algorithm [**?**] as it demands less position evaluation per iteration and is more efficient to avoid local minimums.

Let us consider a generic optimization case where the unknown vector of dimension n is $\mathbf{x}$ and the function to

minimize is f. The simplex is a matrix of $n+1$ guesses, initially chosen to form a basis of the vector space of dimension $n+1$. Let $\mathbf{S} = (\mathbf{x}_1,...,\mathbf{x}_{n+1})$ be this simplex and $f(\mathbf{S}) = (f(\mathbf{x}_1),...,f(\mathbf{x}_{n+1}))$ be the values of the function f evaluated in $\mathbf{S}$. Finding the vector $\mathbf{x}$ that minimizes f goes through updating the simplex with new vectors giving a smaller criterion value at each iteration. To update the simplex, the steps illustrated for $n=2$ in Fig. 8 are the following.

- Sort $\mathbf{S}$ using the value of $f(\mathbf{S})$ arranged in ascending order and re-number them as $\mathbf{S} = (\mathbf{x}_1,...,\mathbf{x}_{n+1})$.
- Compute the centroid $\bar{\mathbf{x}}$ without the worst point $\mathbf{x}_{n+1}$.
- **Reflection**: Compute the reflection point $\mathbf{x}_r = 2\bar{\mathbf{x}} - \mathbf{x}_{n+1}$. If it verifies $f(\mathbf{x}_1) <= f(\mathbf{x}_r) < f(\mathbf{x}_{n+1})$ then replace the least acceptable guess $\mathbf{x}_{n+1}$ by $\mathbf{x}_r$.
- **Expansion**: If $f(\mathbf{x}_r) < f(\mathbf{x}_1)$, compute the expansion point $\mathbf{x}_e = 3\bar{\mathbf{x}} - 2\mathbf{x}_{n+1}$. If it verifies $f(\mathbf{x}_e) < f(\mathbf{x}_r)$ then replace $\mathbf{x}_{n+1}$ by $\mathbf{x}_e$.
- **Outside contraction**: If $f(\mathbf{x}_r) < f(\mathbf{x}_{n+1})$, compute the outside contraction point $\mathbf{x}_{oc} = 1.5\bar{\mathbf{x}} - 0.5\mathbf{x}_{n+1}$. If it verifies $f(\mathbf{x}_{oc}) < f(\mathbf{x}_r)$ then replace $\mathbf{x}_{n+1}$ by $\mathbf{x}_{oc}$.
- **Inside contraction**: If $f(\mathbf{x}_{n+1}) <= f(\mathbf{x}_r)$, compute the inside contraction point $\mathbf{x}_{ic} = 0.5\bar{\mathbf{x}} + 0.5\mathbf{x}_n$. If it verifies $f(\mathbf{x}_{ic}) < f(\mathbf{x}_{n+1})$ then replace $\mathbf{x}_{n+1}$ by $\mathbf{x}_{ic}$.
- **Shrink**: If none of the new values is acceptable, shrink the simplex with $\mathbf{x}_i = \mathbf{x}_i + 0.5(\mathbf{x}_i - \mathbf{x}_1)$, $i \in (1,...,n)$.
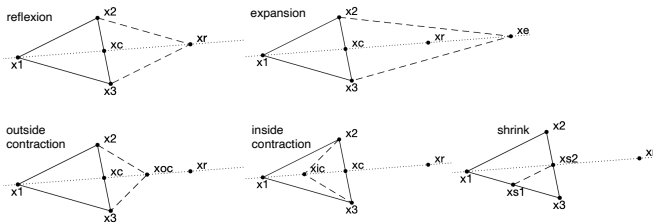- If the simplex vertices are close enough stop the algorithm, else restart.

Fig. 8. Illustration of the main steps in the evolution of the simplex

IV. EXPERIMENTAL VALIDATIONS

This section deals with the assessment of both proposed shape-based estimation schemes (i.e., load-free joint value estimation and external loads estimation). Let us start by introducing the designed experimental platform.

A. Experimental Setup

The experimental setup consists of the TriRod robot and a pair of identical cameras of type UI-3481LE-M-GL with a resolution of 2560×1920 pixels. Each camera is fixed in an eye-to-hand configuration in such a way that they can provide a wide field-of-view of the whole setup (Fig. 9). A calibration procedure is performed to extract both intrinsic and extrinsic parameters of the cameras which are used to build and position the virtual cameras in the SOFA framework visualizing the digital model from the same point-of-view as in the physical setup. Also, an

additional procedure is performed to match the numerical (SOFA) and real model of TriRod. This procedure is used to correct the small potential offset angles due to the imperfections of the robot during its manufacture and assembly, using the estimation loop described in Fig. 6. Finally, the superposition of the model to the images of the TriRod is validated in several known configurations (Fig. 10).
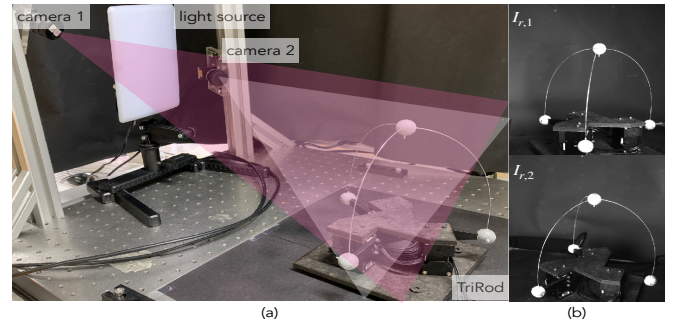

Fig. 9. Overview of the physical setup. (a) shows the TriRod robot and the placement of the cameras and (b) shows an example of pair of images provided by the cameras.
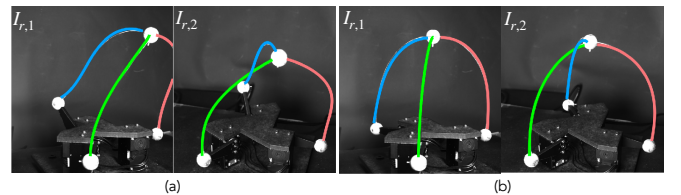

Fig. 10. Superposition of the model shape on images of the real TriRod at: a) input angles of $q = [0,0,0]$ and b) input angles of $q = [0,0,\frac{\pi}{8}]$.

B. Shape-Based Configuration Estimation

As stated in Section III-B, the first proposed method consists of estimating the TriRod actuator configuration by matching the model to the shape of the rods without considering applied external forces. To do this, the robot starts at its initial configuration where all angular positions are at $0°$. The TriRod is then moved step by step to a final random and unknown configuration. At each step, images of the TriRod are acquired with both cameras (Fig. 11). The model is driven with the angle estimation loop (Fig. 6) to match successively the new configurations (Fig. 11(a) to (f)) by minimizing the difference between the projected shape of the model and the images, such that it follows the real TriRod's configuration.

Figure 13 shows five different performed trajectories by the TriRod robot. The robot's shape estimation method provides an average angular error of $1.6°$ for displacements ranging from $0°$ to $75°$, with a minimum error under $0.1°$ and a maximum error of $7.7°$. This leads to a mean percentage error of 3.8% of the norm of each trajectory's final angle.
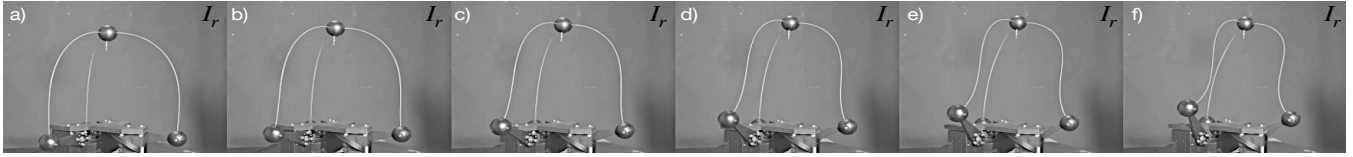
Fig. 11. A sequence of images (only the left-hand images are shown) depicting the different configurations ((a) is the initial position) of the robot that must be reached in order to converge to the final one (f).
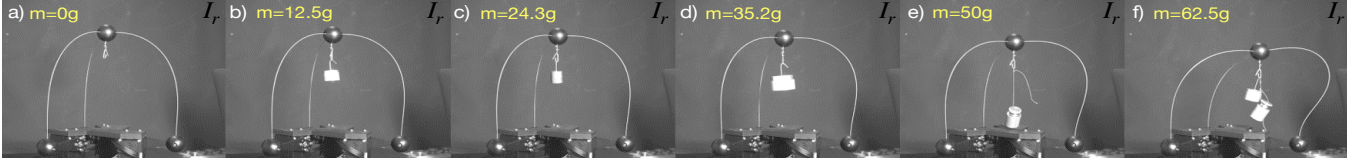

Fig. 12. Images of the different deformation configurations of the TriRod resulting by attaching weights ranging from $0g$ to $62.5g$. The weights are attached to the centre sphere C.
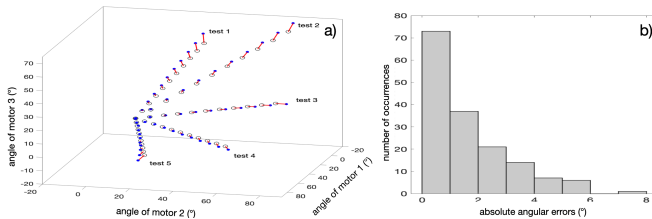

Fig. 13. Joint values estimation results. a) Actuation space where the reference joint values are represented by black circles whereas the corresponding estimated angles are represented by blue dots and the errors are represented by red segments. b) Histogram of the errors for a range of $75°$.
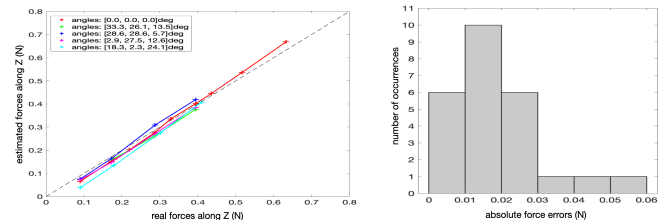

Fig. 14. External load estimation results. a) Estimated forces versus reference applied forces in several angular configurations of the TriRod. b) Histogram of the errors for a range of 0.63 N.

The errors grow linearly as the TriRod reaches extreme positions. Indeed, the further away from the workspace centre the more influential the identification errors are.

C. Shape-Based External Force Estimation

The second proposed estimation scheme is set up at different fixed joint configurations of the TriRod that are chosen randomly but relatively close to the centre. This is necessary so that the TriRod will not collapse under the weight of the upcoming loads. The joint values are first estimated using the method described in Section IV-B such as the model configuration initially matching the load-free shape of the TriRod. The second estimation loop which is represented in Fig. 7 starts when various masses are attached to the end effector, generating a force along Z-axis and implying deformations of the three rods (Fig. 12). This validation focuses on forces along Z-axis because it is the direction of the load of an object to pick and place. In addition to being the most common direction, it is also more convenient to have a precise ground truth as a simple hanged weight. However, external forces along any other direction could be estimated the same way. The resulting new shape of the robot body is considered to be the desired target to estimate the applied external force. Figure 14 shows the estimated force values compared to the real applied forces at five different angular configurations, with three to ten different masses

hanged per configuration. The average error is 20 mN for a range of forces from 90 mN to 633 mN, which corresponds to the range of weights that the TriRod can lift with this design. The maximum error is 52 mN while the minimum error is 1 mN. The overall percentage error is of 10.5%.

The deformation amplitude of the rods is the main source to evaluate the external load. Therefore, there is a trade-off between the range of load that the robot can withstand and the resolution of the load estimation. A stiffer robot can handle greater forces but will be less subject to deformations. Consequently, the load estimation will have a larger range but with a lower resolution. Conversely, a more flexible robot can support only small weights but will generate larger deformations and hence the estimation method will be more sensitive to small weights in a shorter range.

V. DISCUSSIONS

The aim of this study is to introduce a robust model-based force estimation method for a novel parallel continuum robot called TriRod relying on visual feedback comparison with its model. Although the method has demonstrated promising performance under specific conditions, it has certain limitations that require further consideration for future enhancements. Specifically, vision-based sensing may introduce uncertainties coming from occlusions or lighting conditions. To address these challenges, alter-

native sensing techniques, including deformation sensors, magnetic sensors, or actuators' torque sensors, could be used to reinforce the vision-based approach. Furthermore, the current method has solely been evaluated on the TriRod as designed. By introducing alternative geometrical parameters and materials, the TriRod's acceptable ranges of motion and load can be modified, leading to a re-configuration of the workspace and stiffness distribution. Thereby this force estimation method must be set against the current experimental setup.

VI. Conclusion

In this letter, a three DoFs parallel continuum robot called TriRod has been designed, modelled and controlled. The proposed robot consists of three deformable legs (rods), each individual rod is attached at its lower extremity to an angular actuator when the three rods are fixed on a sphere which forms the mobile platform of the robot. A FEM-based method using SOFA framework is used to model the whole robotic structure. A kinematic analysis of the working space and stiffness has been performed showing the relevance of such an architecture in the case of positioning tasks and force sensing.

Two vision-based estimation strategies have been evaluated experimentally. The first proposed method was able to estimate the angular position of the actuators with an average error of $1.6°$ over a range of $75°$. The second method has shown its ability to estimate the externally applied forces in different directions with an average error of $20mN$. Both methods are based on the use of visual feedback providing the shape of the robot (i.e., leg deformation) during a positioning (respectively, force estimation) task.

The future work will concern investigations of other functionalities and applications of the robot, especially in the context of a haptic interface. The shape-based force estimator developed in this paper is indeed well suited to be the force feedback of a master-slave system between a parallel continuum robot and a haptic device, as any directional forces applied on the end effector can be detected from the shape of the robot.

References

[1] C. E. Bryson and D. C. Rucker, "Toward parallel continuum manipulators," in IEEE Int. Conf. on Rob.s and Auto., 2014, pp. 778–785.

[2] F. Campa, M. Diez, et al., "A 2 dof continuum parallel robot for pick & place collaborative tasks," in Adv. in Mech. and Mach. Sci.e:, 2019, pp. 1979–1988.

[3] o. Altuzarra, D. Caballero et al., "Position analysis in planar parallel continuum mechanisms," Mech. Mach. Theory, 2019.

[4] K. Nuelle, T. Sterneck et al., "Modeling, calibration, and evaluation of a tendon-actuated planar parallel continuum robot," IEEE Rob. and Auto. Let., vol. 5, pp. 5811–5818, 2020.

[5] B. Mauzé, R. Dahmouche et al., "Nanometer precision with a planar parallel continuum robot," IEEE Rob. and Auto. Let., vol. 5, pp. 3806 – 3813, 2020.

[6] X. Duan, W. Yan, et al., "Analysis and validation of a planar parallel continuum manipulator with variable cartesian stiffness," Mech. and Mach. Theory, vol. 177, p. 105030, 2022.

[7] J. A. Rivera and C. J. Kim, "Spatial parallel soft robotic architectures," in IEEE/RSJ Int. Conf. on Intel. Rob. and Sys., 2014, pp. 548–553.

[8] G. Böttcher, S. Lilge et al., "Design of a reconfigurable parallel continuum robot with tendon-actuated kinematic chains," IEEE Rob. and Auto. Let., vol. 6, pp. 1272–1279, 2021.

[9] H. Chen, Y. Kang et al., "Kinetostatics modeling and analysis of parallel continuum manipulators," Mech. Mach. Theory, vol. 163, p. 104380, 2021.

[10] X. Huang, X. Zhu et al., "Kinematic modeling and characterization of soft parallel robots," IEEE T. on Rob., 2022.

[11] A. L. Orekhov, C. B. Black et al., "Analysis and validation of a teleoperated surgical parallel continuum manipulator," IEEE Rob. and Auto. Let., vol. 1, pp. 828–835, 2016.

[12] E. M. Young and K. J. Kuchenbecker, "Implementation of a 6-dof parallel continuum manipulator for delivering fingertip tactile cues," IEEE Trans. on Hap., vol. 12, pp. 295–306, 2019.

[13] O. F. Gallardo, B. Mauzé et al., "Turning an articulated 3-ppsr manipulator into a parallel continuum robot," in IEEE/RSJ Int. Conf. on Intel. Rob. and Sys., 2021, pp. 4955–4960.

[14] Z. Yang, X. Zhu et al., "Continuum delta robot: A novel translational parallel robot with continuum joints," in IEEE/ASME Int. Conf. on Adv. Intell. Mech., 2018, pp. 748–755.

[15] G. Wu and G. Shi, "Experimental statics calibration of a multi-constraint parallel continuum robot," Mech. and Mach. Theory, vol. 136, pp. 72–85, 2019.

[16] V. Aloi, K. T. Dang et al., "Estimating forces along continuum robots," IEEE Rob. and Auto. Let., vol. 7, pp. 8877–8884, 2022.

[17] Q. Zhao, J. Lai et al., "Shape estimation and control of a soft continuum robot under external payloads," IEEE/ASME T. on Mech., vol. 27, pp. 2511–2522, 2021.

[18] J. Tapia, E. Knoop et al., "Makesense: Automated sensor design for proprioceptive soft robots," Soft Rob., 2020.

[19] Q. Xiao and Y. Chen, "Efficient force estimation for continuum robot," arXiv preprint arXiv:2109.12469, 2021.

[20] O. Al-Ahmad, M. Ourak et al., "Fbg-based estimation of external forces along flexible instrument bodies," Front. in Rob. and AI, vol. 8, 2021.

[21] M. Jolaei, A. Hooshiar et al., "Sensor-free force control of tendon-driven ablation catheters through position control and contact modeling," in Int. Conf. of the IEEE Eng. in Med. and Biol. Soc., 2020, pp. 5248–5251.

[22] H. Yuan, P. W. Y. Chiu et al., "Shape-Reconstruction Based Force Sensing Method for Continuum Surgical Robots with Large Deformation," IEEE Rob. And Auto. Let., 2017.

[23] H. Guo, F. Ju et al., "Continuum robot shape estimation using permanent magnets and magnetic sensors," Sens. and Actua. A: Physical, vol. 285, pp. 519–530, 2019.

[24] V. K. Venkiteswaran, J. Sikorski et al., "Shape and contact force estimation of continuum manipulators using pseudo rigid body models," in Mech. Mach. Theory, 2019, pp. 34–45.

[25] J. Till, V. Aloi et al., "Real-time dynamics of soft and continuum robots based on Cosserat rod models," Int. J. of Rob. Res., 2019.

[26] M. A. Diezinger, B. Tamadazte et al., "3d curvature-based tip load estimation for continuum robots," IEEE Rob. and Auto. Let., vol. 7, pp. 10 526–10 533, 2022.

[27] A. Hooshiar, A. Sayadi et al., "Accurate estimation of tip force on tendon-driven catheters using inverse cosserat rod model," in Int. Conf. on Biom. Innov. and Appl.), 2020, pp. 37–40.

[28] Z. Zhang, A. Petit et al., "Calibration and external force sensing for soft robots using an rgb-d camera," IEEE Rob. and Auto. Lett., vol. 4, no. 3, pp. 2356–2363, 2019.

[29] J.-P. Merlet, Parallel robots. Springer, 2006, vol. 128.

[30] E. Coevoet, T. Morales-Bieze et al., "Software toolkit for modeling, simulation and control of soft robots," Adv. Rob., vol. 31, pp. 1208–1224, 2017.

[31] C. Duriez, S. Cotin et al., "New approaches to catheter navigation for interventional radiology simulation," Computer Aided Surgery, vol. 11, no. 6, pp. 300-308, 2006.

[32] C. E. Shannon, "A mathematical theory of communication," ACM SIGMOBILE mobile computing and communications review, vol. 5, pp. 3–55, 2001.

[33] J. A. Nelder and R. Mead, "A Simplex Method for Function Minimization," The Comput. J., vol. 7, p. 308–313, 1965.